Geophysical Research Letters

RESEARCH LETTER
10.1029/2019GL085412

Anthropogenic Air Pollution Delays Marine Stratocumulus Breakup to Open Cells

Tom Goren[1,2], **Jan Kazil**[1,2], **Fabian Hoffmann**[1,2], **Takanobu Yamaguchi**[1,2], **and Graham Feingold**[2]

[1]Cooperative Institute for Research in Environmental Sciences, University of Colorado, Boulder, CO, USA, [2]Chemical Sciences Division, NOAA Earth System Research Laboratory, Boulder, CO, USA

Key Points:
- Marine stratocumulus cloud breakup time is systematically delayed with increasing initial background aerosol concentration
- Cloud cover response to aerosol is not saturated, in contrast to the effect of aerosol on cloud albedo at fixed cloudiness
- Realistic Lagrangian large eddy simulations identify the roles of both aerosol and meteorology in determining cloud breakup time

Supporting Information:
- Supporting Information S1
- Movie S1

Correspondence to:
T. Goren,
tom.goren@noaa.gov

Citation:
Goren, T., Kazil, J., Hoffmann, F., Yamaguchi, T., & Feingold, G. (2019). Anthropogenic air pollution delays marine stratocumulus break-up to open-cells. *Geophysical Research Letters*, *46*, 14,135–14,144. https://doi.org/10.1029/2019GL085412

Received 13 SEP 2019
Accepted 5 NOV 2019
Accepted article online 11 NOV 2019
Published online 6 DEC 2019
Corrected 30 DEC 2019

This article was corrected on 30 DEC 2019. See the end of the full text for details.

©2019. American Geophysical Union. All Rights Reserved.

Abstract Marine stratocumulus cloud (Sc) decks with high cloud fraction typically breakup when sufficient drizzle forms. Cloud breakup leads to a lower cloud radiative effect due to the lower cloud amount. Here we use realistic Lagrangian large eddy simulations along a 3-day trajectory, evaluated with satellite observations, to investigate the timing of Sc breakup in response to aerosol conditions. We show that the timing of the breakup is strongly modulated by the diurnal cycle and large-scale meteorology but varies systematically with the initial aerosol concentration: the more polluted the clouds, the later the breakup. This indicates that the cloud radiative effect via cloud cover adjustments is not saturated, in contrast to the effect of aerosol on cloud albedo at fixed cloudiness, which weakens with increasing aerosol levels. The results also show that the cloud radiative impact of anthropogenic aerosol is strongest far from its origin over land.

Plain Language Summary Marine stratocumulus clouds (Sc) cover large areas of the subtropical oceans. They frequently form as fully overcast cloud decks near the western coasts of continents, and break up as they move westwards, driven by the prevailing winds, towards the remote ocean. Their breakup is accompanied by a reduction in cloud cover, which in turn reduces the amount of solar radiation that is reflected by the cloud deck. Aerosol particles, as well as meteorological factors, determine the time it takes for a fully overcast cloud deck to break up. Here we use high-resolution simulations of Sc combined with satellite observations to investigate the roles of aerosol and meteorology in Sc break-up time and location. We demonstrate that an observed Sc deck off the coast of Western Europe would have broken up sooner had it not been influenced by anthropogenic aerosol from Europe. Aerosol was the main factor determining the break-up time of the cloud deck, with a sometimes significant contribution by largescale meteorology. Our results show that even at present-day pollution levels, aerosol perturbations can extend the lifetime of the Sc deck in its overcast state, and exert a significant cooling effect.

1. Introduction

The effect of atmospheric aerosol particles on cloud albedo and coverage is one of the largest sources of uncertainty in climate projections (Boucher et al., 2013). For hypothetical, fixed cloud amounts, the aerosol effect on cloud albedo becomes smaller when the reference background is more polluted (Twomey, 1977). It has therefore been proposed that adding aerosol to present day, already high aerosol levels would result in small changes to cloud albedo (Carslaw et al., 2013; Stevens, 2013). However, the response of changes in cloud amount—broadly speaking, cloud fraction (CF) and liquid water path (LWP; referred to as rapid adjustments; Boucher et al., 2013)—does not necessarily exhibit a saturated response to aerosol perturbations. Marine stratocumulus clouds (Sc) are highly sensitive to such adjustments as typical cloud cover varies between being either fully overcast (closed cells) or broken (open cells, with a typical CF≤65 %) (Atkinson & Zhang, 1996; Goren & Rosenfeld, 2014; Muhlbauer et al., 2014). The large change in CF upon transition between the cloud cover regimes exerts a large cloud radiative effect (CRE) (Goren & Rosenfeld, 2014), with a relatively small contribution from the cloud albedo changes at fixed cloud amount (Chen et al., 2014; Goren & Rosenfeld, 2014).

Sc covers extensive regions over the eastern parts of the major subtropical oceans (Klein & Hartmann, 1993; Muhlbauer et al., 2014). These regions are characterized by decks of closed cells that form near the coast and breakup into open cells and trade wind cumulus as they move westward towards the remote oceans

(Atkinson & Zhang, 1996; Muhlbauer et al., 2014). Observational (Sharon et al., 2006; Stevens et al., 2005; Wood & Hartmann, 2006; Wood et al., 2011) and modeling (Berner et al., 2013; Kazil et al., 2014; Savic-Jovcic & Stevens, 2008; Xue et al., 2008; Wang & Feingold, 2009; Yamaguchi & Feingold, 2015; Yamaguchi et al., 2017) studies have shown that the onset of precipitation is the primary factor in the chain process that leads to the breakup of the fully overcast closed cells: Once in the precipitating state, the Sc system transitions from a primarily top-down driven closed-cell circulation to a bottom-up driven cumulus cloud state (Berner et al., 2011; Feingold et al., 2010; Wang et al., 2010). As the precipitating cumulus cloud elements grow vertically and become more dominant, the overcast layer dissipates and is rapidly replaced by precipitating open cells. Thus, the cloud breakup is the last stage of the transition process. Aerosol, among other factors such as sea surface temperature, boundary layer deepening, entrainment, and free tropospheric (FT) humidity along the cloud trajectory, can promote or inhibit precipitation formation and therefore also the timing of the Sc breakup. Untangling the role of aerosol and large-scale conditions on cloud adjustments, as well as investigating their covariability, is the focus of recent studies (Gryspeerdt et al., 2016; Mülmenstädt & Feingold, 2018).

The prevalence of the Sc decks downwind of the major continents expose them to the influence of continental and anthropogenic aerosol (Adebiyi et al., 2015; Adebiyi & Zuidema, 2018; Allen et al., 2011; George et al., 2013; Goren & Rosenfeld, 2015; Schwartz et al., 2002; Saide et al., 2012; Yang et al., 2011). Using a chemistry and aerosol transport model, colocated with satellite observations, Goren & Rosenfeld (2015) (hereafter GR15) related a long-lived extensive overcast Sc deck to air pollution originating in Western Europe. They showed that the complete breakup of the overcast closed-cell cloud deck occurred 3 days after its formation and only after the cloud drop concentration (N_d) was reduced sufficiently to allow precipitation. It was hypothesized that the higher level of anthropogenic aerosol inhibited precipitation over these 3 days, thereby delaying the closed-cell breakup and inducing a large local radiative forcing, mainly due to the larger CF. Had the air mass not been influenced by anthropogenic air pollution, would the overcast closed cell have broken up sooner?

In the current work, we use realistic Lagrangian large eddy simulation (LES), evaluated by observations, to address the above question and to explore the underlying processes in closed- to open-cell transitions and their radiative impact.

2. Data and Methodology

2.1. Simulation

We developed a new methodology to simulate boundary layer clouds. The approach, realistic Lagrangian LESs, allows for enhanced realism of simulated cloud properties and cloud state evolution relative to observations over periods of days. We employ the System for Atmospheric Modeling (Khairoutdinov & Randall, 2003) as a LES model. We operate the model so that the simulation domain follows a given air mass in the boundary layer, along its Lagrangian trajectory. The model simulates the evolution of the cloud deck embedded in the airmass. Trajectories are determined with the HYSPLIT model (Hybrid Single Particle Lagrangian Integrated Trajectory Model Stein et al., 2015; Rolph et al., 2017) from the fifth generation of the European Centre for Medium-Range Weather Forecasts atmospheric reanalyses (ERA5) reanalysis data (Hersbach, 2018). The trajectories are located 500 m above sea level, at some distance from shear effects near the surface and the inversion. The ERA5 reanalysis provides the mean state of the atmosphere as well as sea surface temperature along the trajectory. We use Newtonian relaxation to nudge mean FT temperature and water vapor in the LESs towards the ERA5 reanalysis, at altitudes 300 m above the simulated inversion, with a nudging time constant of 1,800 s. The mean horizontal wind speed is nudged towards ERA5 at all levels.

The horizontal (vertical) domain size is 76.8 × 76.8 km (5,000 m). A sufficiently large horizontal domain size allows capturing mesoscale organization of the open- (Feingold et al., 2010) and closed-cell SC cloud state (Kazil et al., 2017). The horizontal grid spacing is 200 m. The vertical grid spacing for the simulation presented here is 20 m between 0 and 890 m, 10 m between 890 and 1,890 m, and coarsens from 10 m by 10% per level between 2,100 and 5,000 m. For additional description of the model setup we refer to section 1 in the supporting information (Iacono et al., 2008; Mlawer et al., 1997; Monin & Obukhov, 1954; Yamaguchi et al., 2011, 2017).

We process the simulated thermodynamic and microphysical quantities for evaluation with satellite data. Cloud water path, rain water path (RWP), and LWP are calculated by vertically integrating cloud water, rain

water, and liquid water, respectively, over locations with the associated optical depth ≥3. Cloud optical depth, rain optical depth, and liquid water optical depth are calculated by sampling locations with the respective optical depth ≥3. The satellite optical depth is sampled in a similar fashion. The hydrometeor effective radius is calculated as the ratio of the third to second moments of the cloud and rain drop size distribution. The third and second moments are integrated over locations with cloud and rain optical thickness ≥3, and over one optical depth below cloud top, before their ratio is taken. N_d at cloud top is calculated as the average over locations with cloud and rain optical thickness ≥3 and over one optical depth below cloud top. The in-cloud N_d is calculated as the average over locations with a cloud water content ≥0.01 g kg^{-1}.

2.2. Satellite Observations

Observed cloud properties were retrieved from the Spinning Enhanced Visible and Infrared Imager (SEVIRI) instrument on board the geostationary Meteosat Second Generation. SEVIRI provides observations with high temporal resolution of 15 min with spatial resolution of 3.5×5.5 km^2 in the northeast Atlantic. We used SEVIRI-based cloud products (CF, cloud optical depth τ_c, drop effective radius r_e, and LWP) generated with the Meteosat Second Generation-Cloud Physical Properties algorithm developed at the Royal Netherlands Meteorological Institute available via http://data.knmi.nl (Roebeling et al., 2006). Moderate resolution imaging spectroradiometer (MODIS) true-color images were provided by the National Aeronautics and Space Administration Earth Observing System Data and Information System available at https://worldview.earthdata.nasa.gov/. In order to reduce uncertainty in cloud property retrieval, pixels having τ_c and r_e smaller than 3 are excluded from the analysis as these retrievals are less reliable (Sourdeval et al., 2015). All cloud retrievals were obtained from single-layer liquid clouds. Cloud droplet number concentration is retrieved using the observed r_e and τ_c (Szczodrak et al., 2001) and by assuming an adiabatic fraction of 0.8 and cloud top temperature and pressure of 275 K and 950 hPa, respectively. Potential uncertainties in N_d arise from the high sensitivity of N_d retrieval to r_e (Grosvenor et al., 2018; Szczodrak et al., 2001), especially when r_e is relatively small. Observations of N_d therefore should be considered rather qualitative. The cloud properties along the trajectory were retrieved from an area covering approximately 100×100 km^2, to be comparable with model domain size.

The HYSPLIT back trajectories deviate from actual boundary layer air mass trajectories. Because the clouds of interest are located close to the interface between the clean and polluted air mass (see Figure 1 top panel), the deviation can locate the area used for averaging of the satellite data partly over the clean air mass. For this reason we constructed back trajectories visually from SEVIRI imagery by tracking cloud features by eye to include only clouds in the polluted, continental air mass. Figures 1a-1f show the observations for both ERA5/HYSPLIT and the visually-determined trajectory. Figures S4 and S11 compare the ERA5/HYSPLIT back trajectories with the visually determined trajectories. Sampling along the visually determined back trajectory captures the time evolution of the simulated cloud properties better, while the overall trend is similar for both sampling approaches.

The LWP$_c$ was calculated as follows: an adiabatic calculation with prescribed cloud base temperature and pressure (5 ° C and 950 hPa, respectively; estimated from the simulated trajectory) was used to generate a liquid water content profile with vertical resolution of 10 m and assuming 80 % adiabaticity. Given the simulated N_d at every time step, N_{d_t}, and for each simulation, a vertical profile of the volume effective radius, r_v, was calculated as: $r_{v_i} = [\mathrm{LWC}_i / (4/3\pi\ \rho_w\ N_{d_t})]^{1/3}$ (Freud & Rosenfeld, 2012), with subscripts i and t indicating the vertical level and LES simulation time step, respectively, and ρ_w being the water density. For converting r_v to r_e we assumed that $r_e = 1.08 r_v$ (Freud & Rosenfeld, 2012). Having derived the vertical profile of r_e, we determined LWP$_c$ to be the LWP at the level where $r_e = 14\ \mu$m.

3. Results

The simulations were run along a 3-day trajectory over the northeast Atlantic Ocean downwind of the coasts of Western Europe, on which closed cells transitioned to open cells (GR15). Figure 1, top panel, shows MODIS true-color images of the Sc for each day of the 3-day event, as well as the trajectory location. Figure 1, lower panel, shows the simulated cloud properties (CF, cloud optical thickness τ_c, effective radius r_e, N_d, LWP, and surface precipitation) along the trajectory for varying initial aerosol concentration, N_{a_i} (NA125 to NA300 in intervals of 25 cm^{-3}). Also shown are the satellite-observed cloud properties along the trajectory. The satellite retrievals of cloud properties are limited to daytime only due to the dependence on solar radiation. The time evolution of the cloud properties for the simulations with N_{a_i} of 200–300 cm^{-3} tracks the

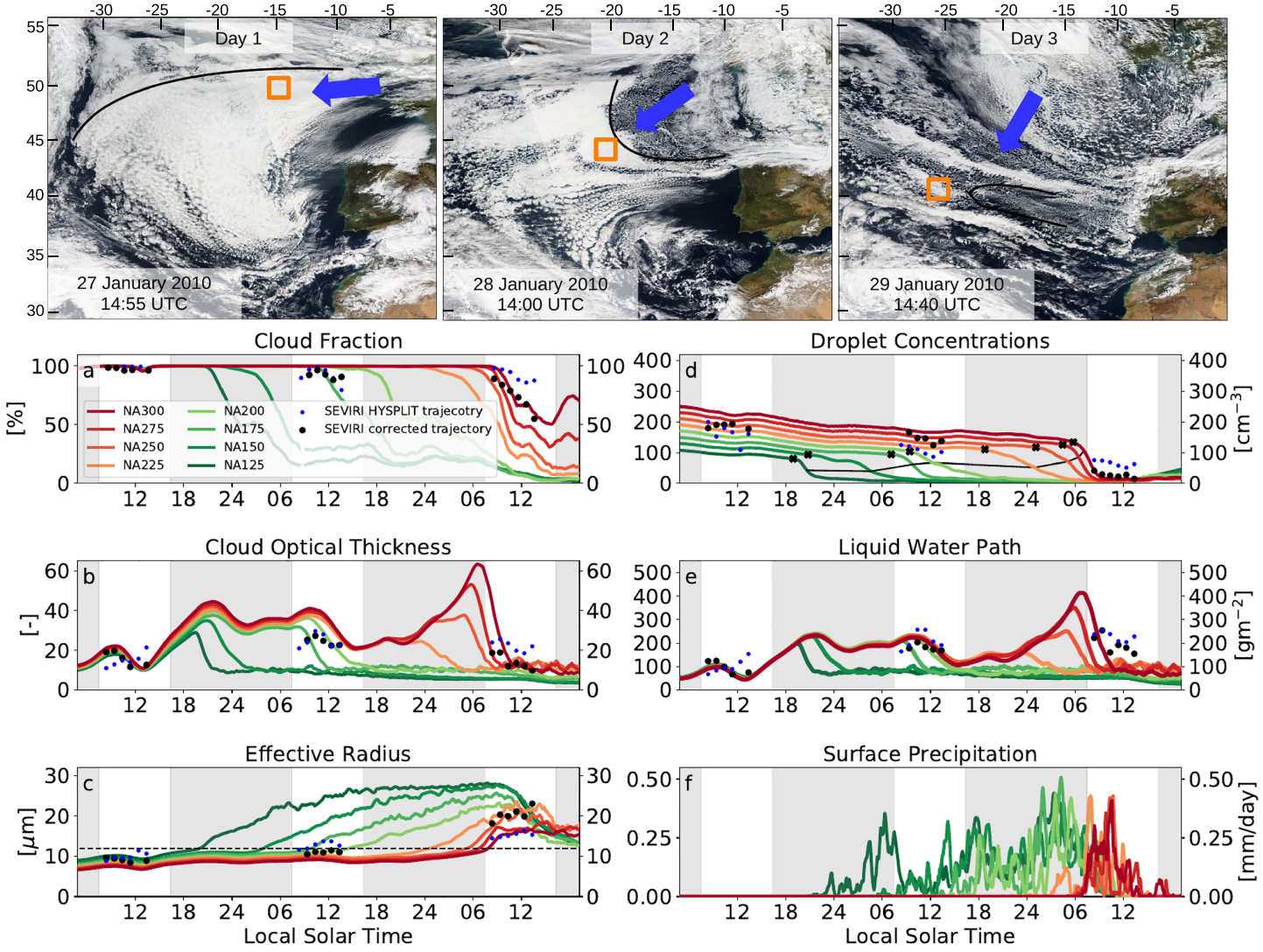

Figure 1. Constraining simulations with observations. Top: MODIS Aqua satellite true-color images of the clouds during the 3-day event. The orange box represents the location of the trajectory at the time of the image, along which clouds were simulated by the large eddy simulation. Arrows indicate the anticyclonic synoptic flow, which was dominated by a stationary high-pressure system causing easterly winds that transported continental air from Europe into the northeast Atlantic Ocean. The vast overcast closed cells on Day 1 covered an area of ~1500 × 1500 km^2 and existed within a plume of air pollution from western Europe (GR15). The black line indicates the border between the polluted European air mass and the maritime pristine air mass, which rotates clockwise along with the anticyclone. The cloud deck started to breakup on Day 2, leaving mostly open cells and remnants of closed cells on Day 3. For a detailed description of the case study, as well as satellite animation, we refer to GR15. Bottom: Time series of selected simulated cloud properties and their comparison with the observations: (a) cloud fraction, (b) τ_c, (c) r_e, (d) N_d, (e) liquid water path, and (f) surface precipitation (observations are not available). Points are the observed cloud properties as retrieved from SEVIRI, blue for the exact trajectory location, and black for the visually determined trajectory (see section 2 for further details). Dashed line in (c) shows $r_e = 12$ μm. Black line in (d) connects the points of maximum scavenging rate ($d^2N_d/dt^2 = 0$) in each simulation. The x symbols indicate the times when rain water path (RWP) >1 g m^{-2}. Gray shading indicates nighttime.

observations reasonably well (Figure 1a–1e), providing confidence that the underlying cloud dynamics and microphysics are captured by the model. In the following, we refer to the simulations with $N_{a_i} < 200$ cm^{-3} as representing Sc clouds with lower degrees of pollution, from which assessments of the Sc breakup times, as well as fundamental features of the system, are derived.

3.1. Cloud Breakup Time Dependence on Initial Aerosol Concentration

We diagnose the closed- to open-cell breakup time based on the CF. As can be seen in Figure 1a, the cloud breakup occurs later for higher N_{a_i}, implying that indeed, under cleaner conditions, the closed cells would breakup sooner. The trajectory follows closed cells that were observed to breakup on Day 3, while its surroundings are already broken (Figure 1; upper panel and GR15). On Day 1 the clouds in the location of the

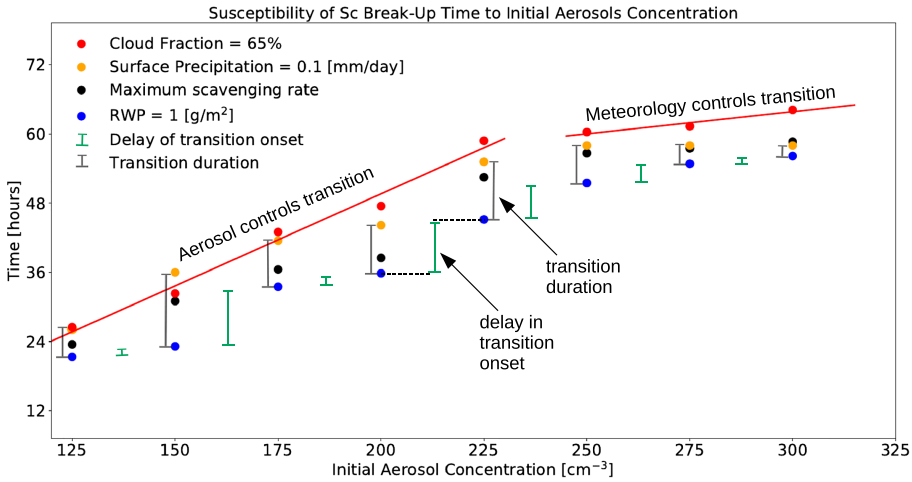

Figure 2. Susceptibility of the Sc transition to N_{a_i}. The processes leading to the cloud breakup are shown: rain drop formation (defined as rain water path [RWP] >1 g m^{-2}; blue) leading to a runaway cleansing of the clouds (represented by $d^2N_d/dt^2 = 0$; black), followed by surface precipitation (>0.1 mm day^{-1}; orange; associated with the beginning of the cloud breakup), and the eventual formation of open cells (defined here as CF≤65 %, red). The staggered vertical green lines represent the *delay in transition onset*, defined as the additional time it takes for the clouds to form rain drops relative to the adjacent, less polluted simulations. The vertical black lines represent the *transition duration*, defined as the time between formation of rain drops to surface precipitation and the associated cloud breakup. The combination of the two time scales results in a systematic delay of the cloud breakup time and open-cell formation with increasing initial N_{a_i}, indicated by a linear interpolation (red line). The two different slopes of the red line are the result of the influence of large scale meteorology (see Figure 3 and text).

trajectory had elevated N_d compared to the surrounding clouds (supporting information Figure S1). Therefore, simulations with lower N_{a_i} can represent trajectories of the nearby less polluted clouds, which breakup sooner.

The closed-cell breakup and emerging spatial organization of the open-cell state is shown in the animated sequence of cloud optical depth (Animation S1). The clearing shown in Animation S1 and Figure 1a proceeds rapidly once surface precipitation begins and accelerates for rates exceeding 0.1 mm day^{-1} (Figures 1f and 2). The formation of surface precipitation occurs simultaneously with r_e, reaching about 12–14 μm, both in the observations and in the simulations (Figure 1c). An r_e of 12–14 μm is a good indicator of significant drizzle (Gerber, 1996; Rosenfeld et al., 2012) and has been shown to be associated with transitions from closed to open cells (Goren & Rosenfeld, 2014; Rosenfeld et al., 2006).

3.2. Cloud Transition Time Scales

Prior to cloud breakup, N_d exhibits two regimes of removal (Figure 1d): (1) a slow decay of N_d followed by (2) a rapid decrease that leads to precipitating open cells and very clean conditions. The existence of the two removal regimes can be explained by the nonlinearity of drizzle formation processes (Gunn & Phillips, 1957); as long as cloud droplets are small, collision-coalescence processes are inefficient and N_d decreases slowly. As the droplets grow and form rain drops (accompanied by the simultaneous rapid increase in r_e; Figure 1c), collision-coalescence accelerates in a positive feedback that accelerates reduction in N_d. This rainout-cleansing process leads eventually to a very clean state with N_d on the order of 10 per cm^{-3} (Figure 1d). As the boundary layer deepens (Figure S2), entrainment of cleaner, FT air dilutes the aerosol concentration, N_a, and can also serve as a significant factor in lowering N_d (Berner et al., 2013; Mechem et al., 2006). Entrainment rates and FT aerosol concentrations can therefore control to some extent the rate of the slow decay regime of N_d, thereby affecting the cloud breakup time (Mechem et al., 2006; Wood et al., 2012; Yamaguchi et al., 2015).

The maximum scavenging rates, defined as d^2N_d/dt^2=0, commensurate with a rapid buildup of rain water mass, are marked in Figure 1d for each of the simulations (black line) and replotted against N_{a_i} in Figure 2. Also shown in Figure 2 are the times of selected key physical processes leading to cloud breakup. These illustrate the chronological order in which the cloud transition occurs: (1) initial formation of rain drops; (2) rapid scavenging of N_d; (3) surface precipitation, which is associated with the beginning of the cloud breakup (Figure 1a and 1f); and (4) formation of open cells, defined here as CF≤65 % (a typical CF for open cells Goren & Rosenfeld, 2014; Muhlbauer et al., 2014). This emphasizes that the breakup becomes possible

only when clouds start to precipitate heavily enough (surface precipitation rates of 0.1 mm day^{-1}; Figure 2), and N_a become sufficiently low, in agreement with previous studies (Berner et al., 2013; Stevens et al., 2005; Wang & Feingold, 2009).

The green and black vertical lines in Figure 2 introduce the *delay in transition onset* and *transition duration* time scales, respectively, which together determine the cloud breakup time. The delay in transition onset is the additional time it takes to begin buildup of rain water, here defined as RWP$_c$ >1 g m^{-2} (blue symbols in Figure 2), from one simulation to its adjacent one with larger N_{a_i}. The transition duration is defined here as the time between RWP$_c$ and the formation of surface precipitation exceeding 0.1 mm day^{-1} (blue and orange symbols, respectively, in Figure 2). A systematic delay in transition onset, and the commensurate cloud break-up, can be seen with higher N_{a_i}. This can be explained based on the dependence of drizzle formation on both N_d and LWP (Berner et al., 2013; Comstock et al., 2004; Freud & Rosenfeld, 2012; Mechem et al., 2012; Pawlowska, 2003; Terai et al., 2012; Yamaguchi & Feingold, 2015).

$$q_l \propto r_e^3 N_d, \tag{1}$$

with q_l being the adiabatic cloud water content at cloud top. Using

$$q_l^2 \propto LWP_{adi}, \tag{2}$$

with LWP$_{adi}$ the adiabatic LWP (see supporting information) and combining (1) and (2) gives

$$LWP_{adi} \propto r_e^6 N_d^2. \tag{3}$$

By assuming a critical r_e of 12–14 μm for initiation of drizzle (Gerber, 1996), r_{e_c}, one can assign an equivalent theoretical critical LWP for breakup, LWP$_c$.

$$LWP_c \propto r_{e_c}^6 N_d^2. \tag{4}$$

Equation (4) expresses a quadratic relationship between LWP$_c$ and N_d. Thus for a given LWP, polluted clouds would require a higher LWP$_c$ and form precipitation later than cleaner clouds (Freud & Rosenfeld, 2012; Konwar et al., 2012), in accordance with our simulations.

3.3. Meteorology Versus Aerosols in Controlling Cloud Breakup Time

Figure 3a illustrates the microphysical processes (manifested by changes in N_d) and large-scale meteorology (manifested by changes in LWP) that together determine the time when the actual LWP = LWP$_c$ (equation 4). Theoretical curves of LWP$_c$ were calculated based on the simulated N_d at every time step (colored lines in 3a). They represent processes that are responsible for reducing N_d (e.g., slow scavenging rate and dilution with FT air), which slowly lower LWP$_c$ with time. Also shown is a time series of the LWP for NA300 (blue line in 3a), which is the last to breakup and therefore provides an envelope LWP that is similar in all simulations up to the onset of the transition processes (see also Figure 1e). The LWP associated with NA300 thus represents large-scale meteorology and diurnal cycle. When the LWP$_c$ and the LWP associated with NA300 intercept, surface precipitation forms (roughly when the simulated r_e is about 12 μm) and the breakup takes place. Equation (4) thus successfully identifies the cloud breakup time based on the meteorological and aerosol state of the system and may serve as a diagnostic for Sc breakup to open cells in global climate models (GCMs).

Evidence for the strong role of meteorology is the rapid increase in LWP on Day 3 (Figure 1e), which is associated with a FT moist layer making contact with the deepening boundary layer (Figures S3 and S2). This allows the LWP of NA250–NA300 to reach LWP$_c$ faster and to form precipitation that eventually breaks up the clouds. An additional set of simulations was performed along a second trajectory of transitioning closed cells originating nearby and having roughly similar N_a on Day 1 but which takes a different path and breaks up a day sooner. A similar systematic response of breakup time versus N_{a_i} was found but with shorter delay times due to a more dramatic water vapor intrusion from the FT. Analysis of this case can be found in the supporting information (section S2 and Figures S7–S11).

Figure 3b shows the NA300 LWP tendency, in which changes in LWP driven by the diurnal cycle are embedded within changes in LWP driven by the large scale meteorology. Whether the LWP increases or decreases,

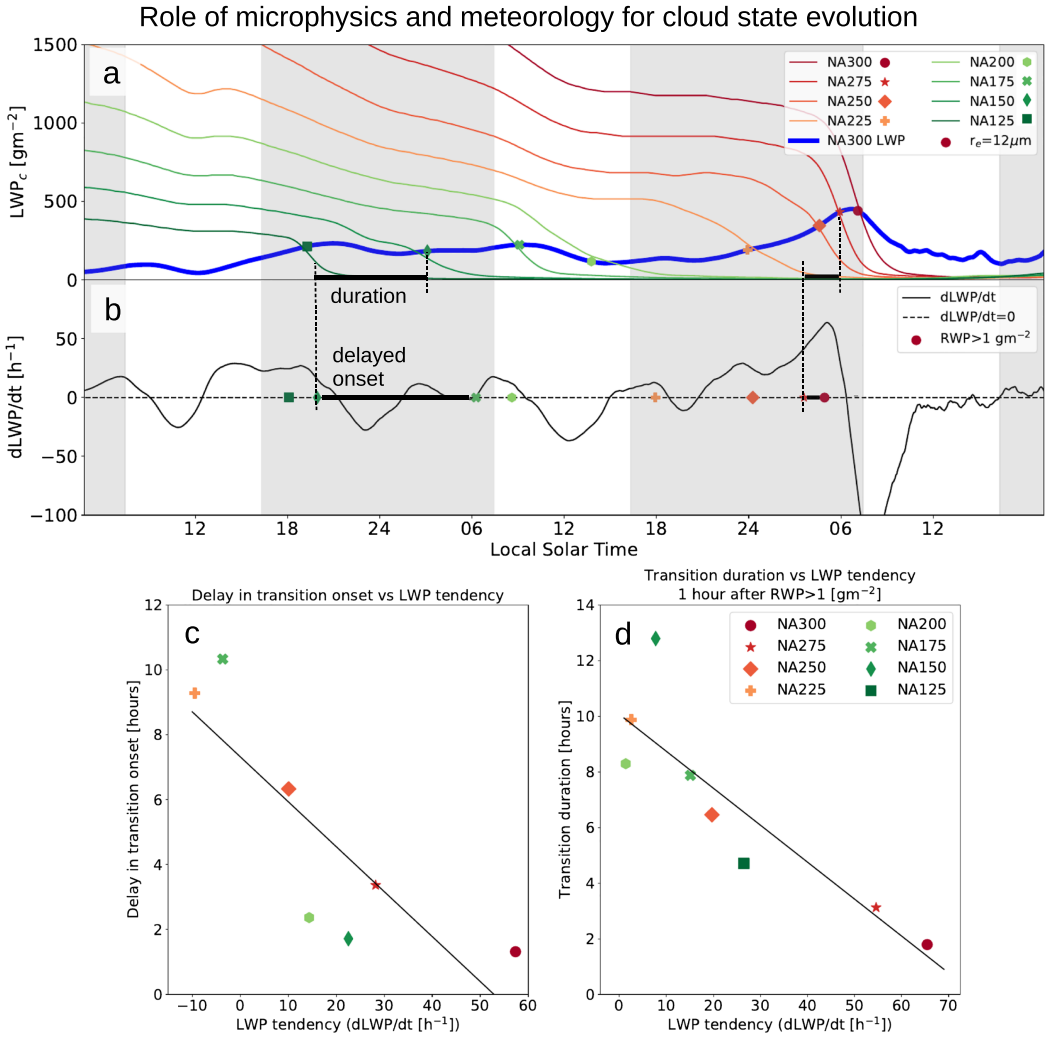

Figure 3. Illustration of the microphysical processes (manifested by changes in N_d) and large-scale meteorology and diurnal cycle (manifested by changes in liquid water path [LWP]) in codetermining the cloud state evolution. (a) Time series of LWP of the NA300 simulation and the theoretical critical LWP for each initial N_{a_i} simulation, LWP$_c$ (equation 4), for which $r_e = 14$ μm, when precipitation often exists and cloud breakup is anticipated. Symbols represent the local time when the simulated $r_e = 12$ μm is reached and precipitation forms (each symbol and color represents each case, e.g., red points represent NA300). An r_e in the range of 12–14 μm is an indicator of significant drizzle (Gerber, 1996; Rosenfeld et al., 2012). (b) The tendency of NA300 LWP (black line) with symbols representing rain water path (RWP)$_c$, the transition onset time (similar convention as in panel a). The quadratic relationship between LWP$_c$ and N_d (see text) explains the systematic delay in transition onset. Decreases in LWP (i.e., negative tendencies) can lengthen the delay in transition onset and transition duration (e.g., see illustration for NA150), while rapid increases (i.e., positive LWP tendencies) make them shorter (e.g., see illustration for NA275). Gray shading in a and b indicates nighttime. (c) Correlation between delay in transition onset and LWP tendency (R^2=0.69). (d) Correlation between transition duration and LWP tendency for a period of 1 hr after RWP$_c$ is reached (R^2 = 0.76).

hastens or dampens precipitation formation processes, thereby affecting the transition onset time and duration and the resultant breakup time. The symbols in Figure 3b represent the transition onset (RWP = RWP$_c$) for each simulation. The delay in transition onset can be inferred from the times at which adjacent simulations (in terms of N_{a_i}) first form an RWP$_c$. The transition duration corresponds to the period between RWP$_c$ in Figure 3b to the time at which r_e reaches 12 μm in Figure 3a. The two time scales are illustrated in Figures 3a and 3b for NA150 and NA275, respectively. The delay in transition onset and the transition duration were found to be anticorrelated with the LWP tendency (Figures 3c and 3d, corresponding to R^2 of 0.69 and 0.76, respectively), which greatly modulates the breakup time due to N_{a_i}. Nevertheless, even within the variability of LWP, greater N_{a_i} systematically delays the cloud breakup (Figure 2, red lines).

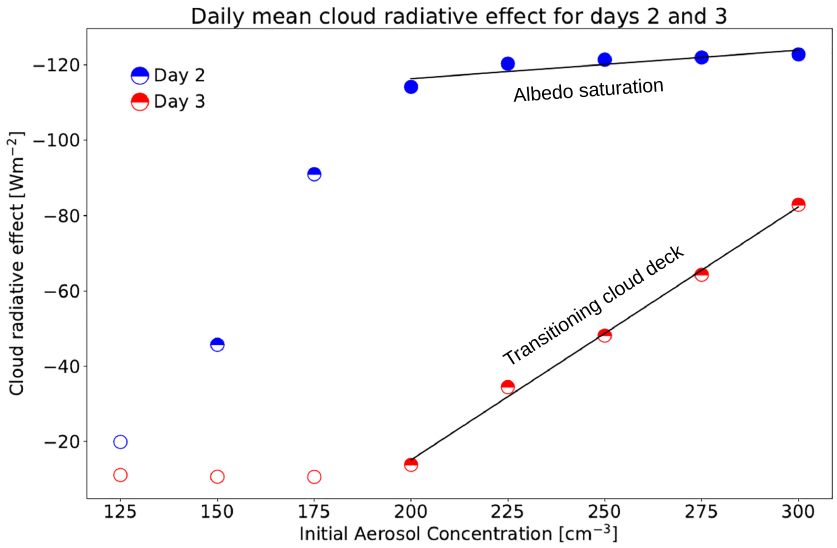

Figure 4. Saturation in the cloud radiative effect (CRE). Simulated daily mean CRE for Days 2 (blue) and 3 (red) of the event. Filled, half-filled, and open symbols represent closed cells, transitioning clouds, and open cells, respectively. Day 2 exhibits saturation in the CRE with increasing initial N_a , while Day 3 shows lack of saturation. The lack of saturation becomes detectable only on Day 3 due to the delayed closed-cell breakup. This emphasizes the role of cloud cover adjustment to aerosol, which translates to large CRE.

4. Summary

In this study, we have identified causal relationships between initial aerosol concentration N_{a_i}, meteorology, and cloud breakup time in LES. We have shown that the delay of cloud breakup due to additional aerosol is modulated by changes in LWP driven by large-scale meteorology and the diurnal cycle. Together, they determine the onset of the transition process, as well as its duration. The breakup time varies systematically with N_{a_i} so that the greater N_{a_i}, the later the breakup occurs. This means, that for the event studied here, cloud cover adjustments to aerosol are not saturated, in contrast to the cloud albedo response to aerosol at fixed cloud amount, which weakens as the background aerosol levels are increased. This is shown in Figure 4, where the daily mean shortwave CRE in the LES is plotted as a function of N_{a_i} for the last 2 days of the simulations. The CRE is nearly saturated on Day 2 for $N_{a_i} > 200$ cm^{-3}, in line with the logarithmic nature of the cloud albedo response to aerosol (Twomey, 1977). On Day 3 on the other hand, CF responds strongly to additional N_{a_i}, driving a commensurate response in the CRE.

Our results imply that the cloud radiative forcing due to cloud cover adjustments to aerosol in polluted Sc decks may well be found over the westernmost parts of the overcast decks, unintuitively far from anthropogenic aerosol sources. Assessing the global significance requires quantifying the frequency of occurrence of interactions between anthropogenic aerosol and Sc susceptible to transition. In order to do so, developing observational methods and strategies is required. GCMs could also be used; however, shallow clouds and their adjustments to aerosol are poorly represented in current models (Ghan et al., 2016; Malavelle et al., 2017; Neubauer et al., 2014). Improving shallow cloud representation in GCMs, and in particular Sc cloud cover adjustments to aerosol, is therefore vital to reducing uncertainty in climate projections.

Acknowledgments
T. G. acknowledge the funding by the Deutsche Forschungsgemeinschaft (DFG, German Research Foundation) Project 268020496-TRR 172, within the Transregional Collaborative Research Center "ArctiC Amplification: Climate Relevant Atmospheric and SurfaCe Processes, and Feedback Mechanisms (AC)^3" during his stay in Leipzig University. Satellite and reanalysis data that were used in this study are available to download per request by the following online ordering data systems: MODIS true-color images(https://worldview.earthdata.nasa.gov/); KNMI MSG-CPP (https://data.knmi.nl); ECMWF ERA5 (https://www.ecmwf.int/en/forecasts/datasets/reanalysis-datasets/era5); and HYSPLIT back trajectories (https://www.ready.noaa.gov/HYSPLIT.php). Simulation results are available at http://esrl.noaa.gov/csd/groups/csd2/clouds. The authors acknowledge the NOAA Research and Development High Performance Computing Program for providing computing and storage resources that have contributed to the research results reported within this paper.

References

Adebiyi, A. A., Zuidema, P., & Abel, S. J. (2015). The Convolution of Dynamics and Moisture with the Presence of Shortwave Absorbing Aerosols over the Southeast Atlantic. *Journal of Climate*, *28*(5), 1997–2024. https://doi.org/10.1175/JCLI-D-14-00352.1

Adebiyi, A. A., & Zuidema, P. (2018). Low Cloud Cover Sensitivity to Biomass-Burning Aerosols and Meteorology over the Southeast Atlantic. *Journal of Climate*, *31*(11), 4329–4346. https://doi.org/10.1175/JCLI-D-17-0406.1

Allen, G., Coe, H., Clarke, A., Bretherton, C., Wood, R., Abel, S. J., et al. (2011). South East Pacific atmospheric composition and variability sampled along 20 S during VOCALS-REx. *Atmospheric Chemistry and Physics*, *11*(11), 5237–5262. https://doi.org/10.5194/acp-11-5237-2011

Atkinson, B. W., & Zhang, J. (1996). Mesoscale shallow convection in the atmosphere. *Reviews of Geophysics*, *34*(4), 403–431. https://doi.org/10.1029/96RG02623

Berner, A. H., Bretherton, C. S., & Wood, R. (2011). Large-eddy simulation of mesoscale dynamics and entrainment around a pocket of open cells observed in VOCALS-REx RF06. *Atmospheric Chemistry and Physics*, *11*(20), 10,525–10,540. https://doi.org/10.5194/acp-11-10525-2011

Berner, A. H., Bretherton, C. S., Wood, R., & Muhlbauer, A. (2013). Marine boundary layer cloud regimes and POC formation in an LES coupled to a bulk aerosol scheme. *Atmospheric Chemistry and Physics Discussions*, *13*(7), 18,143–18,203. https://doi.org/10.5194/acpd-13-18143-2013

Boucher, O., Randall, D., Artaxo, P., Bretherton, C., Feingold, G., Forster, P., et al. (2013). Clouds and Aerosols. In T. F. Stocker et al. (Eds.), *Climate Change 2013: The Physical Science Basis. Contribution of Working Group I to the Fifth Assessment Report of the Intergovernmental Panel on Climate Change* (pp. 571–657). Cambridge, UK and New York: Cambridge University Press. https://doi.org/10.1017/CBO9781107415324.016

Carslaw, K. S., Lee, L. A., Reddington, C. L., Pringle, K. J., Rap, A., Forster, P. M., et al. (2013). Large contribution of natural aerosols to uncertainty in indirect forcing. *Nature*, *503*(7474), 67–71. https://doi.org/10.1038/nature12674

Chen, Y.-C., Christensen, M. W., Stephens, G. L., & Seinfeld, J. H. (2014). Satellite-based estimate of global aerosol–cloud radiative forcing by marine warm clouds. *Nature Geoscience*, *7*(9), 643–646. https://doi.org/10.1038/ngeo2214

Comstock, K. K., Wood, R., Yuter, S. E., & Bretherton, C. S. (2004). Reflectivity and rain rate in and below drizzling stratocumulus. *Quarterly Journal of the Royal Meteorological Society*, *130*(603), 2891–2918. https://doi.org/10.1256/qj.03.187

Feingold, G., Koren, I., Wang, H., Xue, H., & Brewer, W. A. (2010). Precipitation-generated oscillations in open cellular cloud fields. *Nature*, *466*(7308), 849–852. https://doi.org/10.1038/nature09314

Freud, E., & Rosenfeld, D. (2012). Linear relation between convective cloud drop number concentration and depth for rain initiation. *Journal of Geophysical Research*, *117*, D02207. https://doi.org/10.1029/2011JD016457

George, R. C., Wood, R., Bretherton, C. S., & Painter, G. (2013). Development and impact of hooks of high droplet concentration on remote southeast Pacific stratocumulus. *Atmospheric Chemistry and Physics*, *13*(13), 6305–6328. https://doi.org/10.5194/acp-13-6305-2013

Gerber, H. (1996). Microphysics of Marine Stratocumulus Clouds with Two Drizzle Modes. *Journal of the Atmospheric Sciences*, *53*(12), 1649–1662. https://doi.org/10.1175/1520-0469(1996)053<1649:MOMSCW>2.0.CO;2

Ghan, S., Wang, M., Zhang, S., Ferrachat, S., Gettelman, A., Griesfeller, J., et al. (2016). Challenges in constraining anthropogenic aerosol effects on cloud radiative forcing using present-day spatiotemporal variability. *Proceedings of the National Academy of Sciences*, *113*(21), 5804–5811. https://doi.org/10.1073/pnas.1514036113

Goren, T., & Rosenfeld, D. (2014). Decomposing aerosol cloud radiative effects into cloud cover, liquid water path and Twomey components in marine stratocumulus. *Atmospheric Research*, *138*, 378–393. https://doi.org/10.1016/j.atmosres.2013.12.008

Goren, T., & Rosenfeld, D. (2015). Extensive closed cell marine stratocumulus downwind of Europe-A large aerosol cloud mediated radiative effect or forcing? *Journal of Geophysical Research: Atmospheres*, *120*, 6098–6116. https://doi.org/10.1002/2015JD023176

Grosvenor, D. P., Sourdeval, O., Zuidema, P., Ackerman, A., Alexandrov, M. D., Bennartz, R., et al. (2018). Remote Sensing of Droplet Number Concentration in Warm Clouds: A Review of the Current State of Knowledge and Perspectives. *Reviews of Geophysics*, *56*, 409–453. https://doi.org/10.1029/2017RG000593

Gryspeerdt, E., Quaas, J., & Bellouin, N. (2016). Constraining the aerosol influence on cloud fraction. *Journal of Geophysical Research: Atmospheres*, *121*, 3566–3583. https://doi.org/10.1002/2015JD023744

Gunn, R., & Phillips, B. B. (1957). An experimental investigation of the effect of air pollution on the initiation of rain. *Journal of Meteorology*, *14*(3), 272–280. https://doi.org/10.1175/1520-0469(1957)014<0272:AEIOTE>2.0.CO;2

Hersbach, H. (2018). *Operational global reanalysis: Progress, future directions and synergies with NWP*, European Centre for Medium Range Weather Forecasts.

Iacono, M. J., Delamere, J. S., Mlawer, E. J., Shephard, M. W., Clough, S. A., & Collins, W. D. (2008). Radiative forcing by long-lived greenhouse gases: Calculations with the AER radiative transfer models. *Journal of Geophysical Research*, *113*, D13103. https://doi.org/10.1029/2008JD009944

Kazil, J., Feingold, G., Wang, H., & Yamaguchi, T. (2014). On the interaction between marine boundary layer cellular cloudiness and surface heat fluxes. *Atmospheric Chemistry and Physics*, *14*(1), 61–79. https://doi.org/10.5194/acp-14-61-2014

Kazil, J., Yamaguchi, T., & Feingold, G. (2017). Mesoscale organization, entrainment, and the properties of a closed-cell stratocumulus cloud. *Journal of Advances in Modeling Earth Systems*, *9*(5), 2214–2229. https://doi.org/10.1002/2017MS001072

Khairoutdinov, M. F., & Randall, D. A. (2003). Cloud Resolving Modeling of the ARM Summer 1997 IOP: Model Formulation, Results, Uncertainties, and Sensitivities. *Journal of the Atmospheric Sciences*, *60*(4), 607–625. https://doi.org/10.1175/1520-0469(2003)060<0607:CRMOTA>2.0.CO;2

Klein, S. A., & Hartmann, D. L. (1993). The seasonal cycle of low stratiform clouds. https://doi.org/10.1175/1520-0442(1993)006<1587:TSCOLS>2.0.CO;2

Konwar, M., Maheskumar, R. S., Kulkarni, J. R., Freud, E., Goswami, B. N., & Rosenfeld, D. (2012). Aerosol control on depth of warm rain in convective clouds. *Journal of Geophysical Research*, *117*, D13204. https://doi.org/10.1029/2012JD017585

Malavelle, F. F., Haywood, J. M., Jones, A., Gettelman, A., Clarisse, L., Bauduin, S., et al. (2017). Strong constraints on aerosol–cloud interactions from volcanic eruptions. *Nature*, *546*(7659), 485–491. https://doi.org/10.1038/nature22974

Mechem, D. B., Robinson, P. C., & Kogan, Y. L. (2006). Processing of cloud condensation nuclei by collision-coalescence in a mesoscale model. *Journal of Geophysical Research*, *111*, D18204. https://doi.org/10.1029/2006JD007183

Mechem, D. B., Yuter, S. E., & De Szoeke, S. P. (2012). Thermodynamic and aerosol controls in southeast Pacific stratocumulus. *Journal of the Atmospheric Sciences*, *69*(4), 1250–1266.

Mlawer, E. J., Taubman, S. J., Brown, P. D., Iacono, M. J., & Clough, S. A. (1997). Radiative transfer for inhomogeneous atmospheres: RRTM, a validated correlated-k model for the longwave. *Journal of Geophysical Research*, *102*(D14), 16,663–16,682. https://doi.org/10.1029/97JD00237

Monin, A. S., & Obukhov, A. M. (1954). Basic laws of turbulent mixing in the atmosphere near the ground. *Trudy Geofizicheskogo Instituta, Akademiya Nauk SSSR*, *24*(151), 163–187.

Muhlbauer, A., McCoy, I. L., & Wood, R. (2014). Climatology of stratocumulus cloud morphologies: Microphysical properties and radiative effects. *Atmospheric Chemistry and Physics*, *14*, 6695–6716. https://doi.org/10.5194/acp-14-6695-2014

Mülmenstädt, J., & Feingold, G. (2018). The Radiative Forcing of Aerosol–Cloud Interactions in Liquid Clouds: Wrestling and Embracing Uncertainty. *Current Climate Change Reports*, *4*(1), 23–40. https://doi.org/10.1007/s40641-018-0089-y

Neubauer, D., Lohmann, U., Hoose, C., & Frontoso, M. G. (2014). Impact of the representation of marine stratocumulus clouds on the anthropogenic aerosol effect. *Atmospheric Chemistry and Physics*, *14*(21), 11,997–12,022. https://doi.org/10.5194/acp-14-11997-2014

Pawlowska, H. (2003). An observational study of drizzle formation in stratocumulus clouds for general circulation model (GCM) parameterizations. *Journal of Geophysical Research*, *108*(D15), 8630. https://doi.org/10.1029/2002JD002679

Roebeling, R. A., Feijt, A. J., & Stammes, P. (2006). Cloud property retrievals for climate monitoring: Implications of differences between Spinning Enhanced Visible and Infrared Imager (SEVIRI) on METEOSAT-8 and Advanced Very High Resolution Radiometer (AVHRR) on NOAA-17. *Journal of Geophysical Research*, *111*, D20210. https://doi.org/10.1029/2005JD006990

Rolph, G., Stein, A., & Stunder, B. (2017). Real-time Environmental Applications and Display sYstem: READY. *Environmental Modelling & Software*, *95*, 210–228. https://doi.org/10.1016/j.envsoft.2017.06.025

Rosenfeld, D., Kaufman, Y. J., & Koren, I. (2006). Switching cloud cover and dynamical regimes from open to closed Benard cells in response to the suppression of precipitation by aerosols. *Atmospheric Chemistry and Physics*, *6*(9), 2503–2511. https://doi.org/10.5194/acp-6-2503-2006

Rosenfeld, D., Wang, H., & Rasch, P. J. (2012). The roles of cloud drop effective radius and LWP in determining rain properties in marine stratocumulus. *Geophysical Research Letters*, *39*, L13801. https://doi.org/10.1029/2012GL052028

Saide, P. E., Spak, S. N., Carmichael, G. R., Mena-Carrasco, M. A., Yang, Q., Howell, S., et al. (2012). Evaluating WRF-Chem aerosol indirect effects in Southeast Pacific marine stratocumulus during VOCALS-REx. *Atmospheric Chemistry and Physics*, *12*(6), 3045–3064. https://doi.org/10.5194/acp-12-3045-2012

Savic-Jovcic, V., & Stevens, B. (2008). The Structure and Mesoscale Organization of Precipitating Stratocumulus. *Journal of the Atmospheric Sciences*, *65*(5), 1587–1605. https://doi.org/10.1175/2007JAS2456.1

Schwartz, S. E., Benkovitz, C. M., & Benkovitz, C. M. (2002). Influence of anthropogenic aerosol on cloud optical depth and albedo shown by satellite measurements and chemical transport modeling. *Proceedings of the National Academy of Sciences*, *99*(4), 1784–1789.

Sharon, T. M., Albrecht, B. A., Jonsson, H. H., Minnis, P., Khaiyer, M. M., van Reken, T. M., et al. (2006). Aerosol and Cloud Microphysical Characteristics of Rifts and Gradients in Maritime Stratocumulus Clouds. *Journal of the Atmospheric Sciences*, *63*(3), 983–997. https://doi.org/10.1175/JAS3667.1

Sourdeval, O., Labonnote, L. C., Baran, A. J., & Brogniez, G. (2015). A methodology for simultaneous retrieval of ice and liquid water cloud properties. Part I: Information content and case study. *Quarterly Journal of the Royal Meteorological Society*, *141*(688), 870–882. https://doi.org/10.1002/qj.2405

Stein, A. F., Draxler, R. R., Rolph, G. D., Stunder, B. J. B., Cohen, M. D., & Ngan, F. (2015). NOAA's HYSPLIT Atmospheric Transport and Dispersion Modeling System. *Bulletin of the American Meteorological Society*, *96*(12), 2059–2077. https://doi.org/10.1175/BAMS-D-14-00110.1

Stevens, B. (2013). Uncertain then, irrelevant now. *Nature*, *503*(7474), 47–48. https://doi.org/10.1038/503047a

Stevens, B., Vali, G., Comstock, K., Wood, R., Van Zanten, M. C., Austin, P. H., et al. (2005). Pockets of Open Cells and Drizzle in Marine Stratocumulus. *Bulletin of the American Meteorological Society*, *86*(1), 51–57. https://doi.org/10.1175/BAMS-86-1-51

Szczodrak, M., Austin, P. H., & Krummel, P. B. (2001). Variability of Optical Depth and Effective Radius in Marine Stratocumulus Clouds. *Journal of the Atmospheric Sciences*, *58*(19), 2912–2926. https://doi.org/10.1175/1520-0469(2001)058<2912:VOODAE>2.0.CO;2

Terai, C. R., Wood, R., Leon, D. C., & Zuidema, P. (2012). Does precipitation susceptibility vary with increasing cloud thickness in marine stratocumulus? *Atmospheric Chemistry and Physics*, *12*(10), 4567–4583. https://doi.org/10.5194/acp-12-4567-2012

Twomey, S. (1977). The Influence of Pollution on the Shortwave Albedo of Clouds. *Journal of the Atmospheric Sciences*, *34*(7), 1149–1152. https://doi.org/10.1175/1520-0469(1977)034<1149:TIOPOT>2.0.CO;2

Wang, H., & Feingold, G. (2009). Modeling Mesoscale Cellular Structures and Drizzle in Marine Stratocumulus. Part I: Impact of Drizzle on the Formation and Evolution of Open Cells. *Journal of the Atmospheric Sciences*, *66*(11), 3237–3256. https://doi.org/10.1175/2009JAS3022.1

Wang, H., Feingold, G., Wood, R., & Kazil, J. (2010). Modelling microphysical and meteorological controls on precipitation and cloud cellular structures in Southeast Pacific stratocumulus. *Atmospheric Chemistry and Physics*, *10*(13), 6347–6362. https://doi.org/10.5194/acp-10-6347-2010

Wood, R., Bretherton, C. S., Leon, D., Clarke, A. D., Zuidema, P., Allen, G., & Coe, H. (2011). An aircraft case study of the spatial transition from closed to open mesoscale cellular convection over the Southeast Pacific. *Atmospheric Chemistry and Physics*, *11*(5), 2341–2370. https://doi.org/10.5194/acp-11-2341-2011

Wood, R., & Hartmann, D. L. (2006). Spatial Variability of Liquid Water Path in Marine Low Cloud: The Importance of Mesoscale Cellular Convection. *Journal of Climate*, *19*(9), 1748–1764. https://doi.org/10.1175/JCLI3702.1

Wood, R., Leon, D., Lebsock, M., Snider, J., & Clarke, A. D. (2012). Precipitation driving of droplet concentration variability in marine low clouds. *Journal of Geophysical Research*, *117*, D19210. https://doi.org/10.1029/2012JD018305

Xue, H., Feingold, G., & Stevens, B. (2008). Aerosol Effects on Clouds, Precipitation, and the Organization of Shallow Cumulus Convection. *Journal of the Atmospheric Sciences*, *65*(2), 392–406. https://doi.org/10.1175/2007JAS2428.1

Yamaguchi, T., & Feingold, G. (2015). On the relationship between open cellular convective cloud patterns and the spatial distribution of precipitation. *Atmospheric Chemistry and Physics*, *15*(3), 1237–1251. https://doi.org/10.5194/acp-15-1237-2015

Yamaguchi, T., Feingold, G., & Kazil, J. (2017). Stratocumulus to Cumulus Transition by Drizzle. *Journal of Advances in Modeling Earth Systems*, *9*, 2333–2349. https://doi.org/10.1002/2017MS001104

Yamaguchi, T., Feingold, G., Kazil, J., & McComiskey, A. (2015). Stratocumulus to cumulus transition in the presence of elevated smoke layers. *Geophysical Research Letters*, *42*, 10,478–10,485. https://doi.org/10.1002/2015GL066544

Yamaguchi, T., Randall, D. A., & Khairoutdinov, M. F. (2011). Cloud Modeling Tests of the ULTIMATE–MACHO Scalar Advection Scheme. *Monthly Weather Review*, *139*(10), 3248–3264. https://doi.org/10.1175/MWR-D-10-05044.1

Yang, Q., Fast, J. D., Wang, H., Easter, R. C., Morrison, H., Lee, Y.-N., et al. (2011). Assessing regional scale predictions of aerosols, marine stratocumulus, and their interactions during VOCALS-REx using WRF-Chem. *Atmospheric Chemistry and Physics*, *11*(23), 11,951–11,975. https://doi.org/10.5194/acp-11-11951-2011

Erratum

In the originally published version of this article, there were errors in Figure 3; the Plain Language Summary was also omitted. These errors have since been corrected, and the present version may be considered the authoritative version of record.